Electrochimica Acta 257 (2017) 89–98

Contents lists available at ScienceDirect

Electrochimica Acta

journal homepage: www.elsevier.com/locate/electacta

Research Paper

Phosphoric Acid Invasion in High Temperature PEM Fuel Cell Gas Diffusion Layers

N. Bevilacqua[a], M.G. George[b], S. Galbiati[a], A. Bazylak[b], R. Zeis[a,c,*]

[a] Karlsruhe Institute of Technology (KIT), Helmholtz Institute Ulm (HIU), Helmholtzstraße 11, 89081 Ulm, Germany
[b] Thermofluids for Energy and Advanced Materials (TEAM) Laboratory, Department of Mechanical & Industrial Engineering, University of Toronto Institute for Sustainable Energy, Faculty of Applied Science & Engineering, University of Toronto, 5 King's College Road, Toronto, Ontario, M5S 3G8, Canada
[c] Karlsruhe Institute of Technology (KIT), Institute for Physical Chemistry, Fritz-Haber-Weg 2, 76131 Karlsruhe, Germany

ARTICLE INFO

Article history:
Received 9 June 2017
Received in revised form 8 August 2017
Accepted 7 October 2017
Available online 12 October 2017

Keywords:
high temperature polymer electrolyte membrane fuel cell (HT-PEMFC)
X-ray tomography (μCT)
gas diffusion layer (GDL)
phosphoric acid leaching
injection experiment
pore network modeling

ABSTRACT

In this work, liquid phosphoric acid was injected into polymer electrolyte membrane fuel cell (PEMFC) gas diffusion layers (GDLs) to visualize the invasion patterns developed at breakthrough. Three-dimensional (3D) images of the GDLs were obtained through X-ray computed tomography, and equivalent pore networks were generated as the basis for pore network simulations using OpenPNM. Strong qualitative agreement was obtained between the simulated and experimentally observed liquid phosphoric acid invasion patterns, which provided validation for the numerical modeling. Different GDL materials were evaluated by examining the effects of a micro porous layer (MPL) and pore size distribution on the saturation and distribution of phosphoric acid. The MPL was shown to restrict liquid phosphoric acid from entering the carbon fiber substrate. The overall phosphoric acid saturation at breakthrough was found to decrease significantly for samples containing an MPL due to the smaller pore sizes. Further, the influence of cracks in an MPL on overall saturation at breakthrough was investigated. It was observed that a crack-free MPL provided a more effective physical barrier to restrict the undesired leaching of liquid phosphoric acid through the GDL.

1. Introduction

Polymer electrolyte membrane fuel cells (PEMFCs) are a promising technology for clean energy generation, producing only heat and water as local operational by-products. Typical polymer electrolyte membrane fuel cells operate below 100 °C to facilitate hydration of the Nafion® membranes commonly employed in these fuel cells [1,2]. Operational challenges faced by typical PEMFCs include delicate water management [3,4] and extremely low tolerances towards impurities [5]. Additionally, operating PEMFCs below 100 °C introduces significant mass transport related performance limitations due to the accumulation of liquid water at high current densities.

By increasing the working temperature of a PEMFC above 100 °C, fuel cell tolerance to reactant impurities is improved and water management challenges can be overcome [6,7]. Primarily, mass transport losses associated with liquid water accumulation in the fuel cell are eliminated above the boiling point of water. Additionally, the electrochemical reaction kinetics and the use of steam reformates are facilitated by temperatures between 140 °C and 180 °C [2,8,9].

However, at temperatures above the boiling point of water, hydration of the Nafion is compromised, and fuel cell performance decreases due to insufficient proton conductivity in the membrane [10]. As an alternative to Nafion, the most commonly used membrane for high temperature PEMFC operation is a polybenzimidazole (PBI) film doped with concentrated phosphoric acid [10–12]. Protonic conductivity of the PBI membrane is strongly related to the phosphoric acid content of the membrane [13,14]. The parameters of the PBI-membrane doping process with phosphoric acid, such as immersion time and solution temperature, influence the distribution of phosphoric acid in the membrane by determining the initial concentration of acid within the membrane [15,16]. After construction of the membrane electrode assembly, the initial state of the doped membrane determines how much phosphoric acid migrates from the membrane into the electrodes during the activation phase [17–19]. During the activation phase, phosphoric acid forms the triple-phase boundary at which the electrochemical reaction takes place by invading the catalyst layer [20–23].

* Corresponding author at: Karlsruhe Institute of Technology (KIT), Helmholtz Institute Ulm (HIU), Helmholtzstr. 11, 89081 Ulm, Germany.
E-mail address: roswitha.zeis@kit.edu (R. Zeis).

https://doi.org/10.1016/j.electacta.2017.10.054

During operation, phosphoric acid has been shown to accumulate in the exhaust water, complicating water recycling (exhaust water may require neutralization) and corroding the piping and bipolar plates [24,25]. Understanding the process of phosphoric acid migration during the activation phase as well as minimizing the acid loss during operation would allow for improved high temperature-PEMFC (HT-PEMFC) designs which optimize catalyst utilization to the benefit of overall performance and durability [11,21]. An improved understanding of phosphoric acid migration in HT-PEMFCs may also lead to lower platinum loadings in the catalyst layer, resulting in significant cost reductions [11]. Phosphoric acid leaching from the GDL into the channel and the exhaust water has been investigated by several groups and the results suggest that acid leaching is not a major contributor to long-term voltage degradation [22,23,26].

Previously, the activation phase has been investigated to optimize and understand the initial acid distribution and the development of the triple-phase boundary. Wannek et al. and Eberhardt et al. both found the initial redistribution of phosphoric acid from the PBI-doped membrane to be a quick process (less than 10 minutes), however, several hours were required before a dynamic equilibrium was established. Additionally, the initial amount of phosphoric acid introduced in to the cell (via PBI doping) was found to be a critical factor for maximization of the electrochemically active surface area (ECSA) and optimization of cell performance [22,23].

The capillary dominated flow which is characteristic of phosphoric acid migration in HT-PEMFCs is also characteristic of water transport in low-temperature PEMFCs. In particular, the presence of a microporous layer (MPL) in the GDL has been shown to significantly improve water management and reduce liquid water saturation in operating fuel cells [27,28]. Gostick et al. found the water saturation drastically decreased from 27% to 3% at breakthrough with the application of an MPL. They further postulated that the liquid water transport through the MPL occurred predominantly through cracks in the MPL since similar results were obtained when an otherwise impermeable mask with cracks was placed over the GDL [28–30]. These findings were further supported by Markötter et al. and Sasabe et al. who investigated the liquid water transport through cracks in the MPL. They concluded that liquid water does not reside in the bulk MPL, and they attributed the lack of water to the MPL hydrophobicity and presence of cracks for liquid water transport pathways [31,32]. Mortazavi et al. and Bresciani et al. both observed an increase in the breakthrough pressure by several kPa with the presence of an MPL [3,33], a result that inspired several researchers to investigate the effect of an MPL on phosphoric acid distribution in HT-PEMFC GDLs. The MPL also functions as a structural support for the catalyst layer (CL) and increases the adhesion and the contact area of the electrode layers. Lobato et al. found that an MPL is beneficial to the overall performance of a cell, as it increases the ECSA. These beneficial effects outweigh the additional gas mass transport resistance introduced by an MPL [34].

Furthermore, visualization studies have led to quantified liquid water transport in gas diffusion layer (GDL) materials for low temperature PEMFCs. In particular, to understand the water transport and accumulation in the GDL, ex situ and in situ X-ray [35–37] and neutron imaging [38] based studies have been performed extensively in recent years. However, the application of in situ X-ray imaging is especially complex for HT-PEMFCs, as the dynamic triple-phase boundary and local concentration variations of phosphoric acid during operation change the local beam attenuation over time [15]. Neutron imaging [39], post-mortem acid-base titration [19], voltammetry and electrochemical impedance spectroscopy [18,20,40] based studies have been performed to determine changes in the ECSA. These experimental results constitute a foundation on which theoretical models can be based. Computational fuel cell engineering offers an efficient approach to systematically investigate several different parameters that are otherwise costlier and more time consuming to obtain [41]. Eberhardt et al. and Kim et al. predicted descriptive functions that calculate the lifetime of HT-PEMFCs under various operating conditions [42,43], Baricci et al. created an insightful model to predict EIS spectra [44], and Caglayan et al. developed a demonstrative 3D model to predict polarization curves and investigated the effect of temperature on the operation of a HT-PEMFC [45].

The combination of experiments and modeling is pivotal for solidifying gathered knowledge and complementing stated theories based on experiments. Conventional visualization techniques typically lack in temporal and spatial resolutions to resolve key pore scale transport phenomena in the GDL interior, such as phosphoric acid migration through an MPL [46,47]. Microscale multiphase transport phenomena have been investigated using pore network modeling, a tool which has been proven to be a promising approach for simulating the flow of liquids through GDLs [46–51]. This type of modeling approach provides a useful link between the microscopic and macroscopic features of a GDL, which are conventionally challenging to capture with volume-averaging continuum models [52].

The open source software package OpenPNM is a powerful pore network modeling tool, which has been employed by several research groups in the investigation of fluid distribution processes during fuel cell operation [52]. Gostick et al. created a regular cubic network and a randomly generated network in order to represent their GDLs [50]. Fazeli et al. studied the influence of the number of inlet pores on the overall GDL water saturation [48]. Lastly, to the best of the authors' knowledge, Chevalier et al. was the first group to model the phosphoric acid distribution in a high temperature PEM fuel cell GDL. They found that the MPL restricts the movement of phosphoric acid to the flow fields and acid transport takes place through the cracks inside the MPL [21]. The findings of Chevalier et al. are in good agreement with the experimental results reported by Gostick et al. [28] and Eberhardt et al. [15].

In this work, phosphoric acid transport through the GDL is investigated via ex situ phosphoric acid breakthrough experiments. The effect of an MPL on the distribution of phosphoric acid at breakthrough is investigated and visualized using X-ray micro-computed tomography. Experimentally obtained 3D phosphoric acid breakthrough patterns are then used to validate simulations performed via pore network modeling (using OpenPNM), and a parametric study of GDL network parameters, such as porosity, capillary pressure, and pore size distribution, on the overall distribution of phosphoric acid in the GDL is performed, with particular interest in the effect of the MPL. The methodology for acquiring, reconstructing, and segmenting μCT images of GDLs, as well as the modeling and invasion percolation simulations of 3D pore networks extracted from these materials, will be explored.

2. Methodology

The methodology section of this paper is presented in two major parts. The first of which presents the ex situ injection device used to perform the phosphoric acid breakthrough experiments and details the subsequent acquisition of X-ray micro-computed tomography scans. The second part of the methodology section is focused on the modeling efforts of this study, including pore network extraction and the implementation of OpenPNM to perform invasion percolation studies. A schematic of the experimental setup is shown in Fig. 1.

Four GDL materials were investigated, including Sigracet SGL 25 BA, SGL 25 BC, Freudenberg H2315, and Freudenberg H2315-C2. For

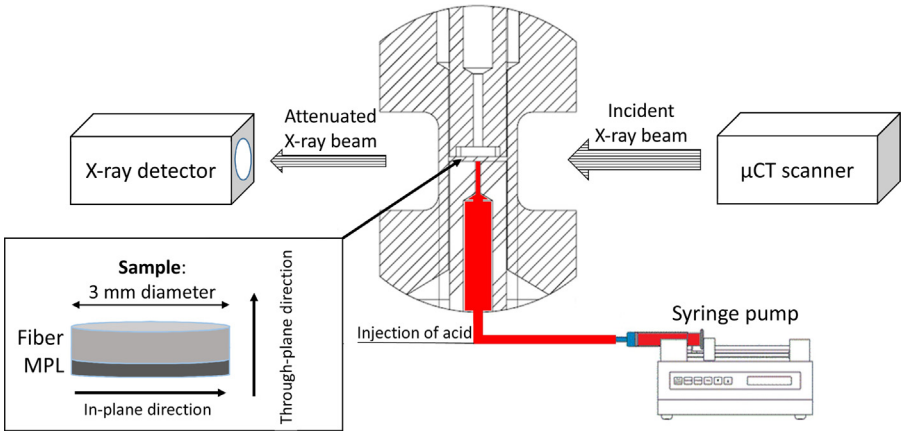

Fig. 1. Schematic representation of the experimental setup used to obtain 3D μCT images of the carbon fiber structure of the investigated materials. The phosphoric acid injection pathway is denoted in red.

the SGL XX YZ materials with a naming convention of XX YZ, XX identifies the substrate as carbon fiber paper, Y identifies the substrate PTFE content (here: 5 wt.% PTFE), Z = C identifies the presence of an MPL coating (here: 23 wt.% PTFE), and Z = A refers to the absence of an MPL. For the Freudenberg materials the additional suffix (C2) identifies the presence of a MPL. It is important to note that both SGL materials and both Freudenberg GDLs have the same carbon fiber substrate structure, respectively.

2.1. Ex situ Injection Experiment

A specialized point injection device was designed and manufactured in-house to perform ex situ breakthrough experiments on GDL materials. The geometry of the device was optimized for compatibility with high resolution X-ray imaging to characterize breakthrough patterns and saturation profiles in the invaded GDLs. The circular geometry of the device facilitates uniform X-ray attenuation behavior for all angular positions of the device. Additionally, excess material was removed from the supporting structures of the device in the sample imaging plane to improve contrast in the GDL.

The point injection device is compatible with 3 mm diameter GDL samples and features a single injection point on the lower face (MPL side), see Fig. 1. The injection point is located at the center of the GDL sample and is 0.25 mm in diameter, representing less than 1% of the GDL sample area. The upper face (carbon fiber substrate side) features a single channel 0.5 mm wide and 2.25 mm long. The compressed thickness of the GDL sample is controlled using rigid polyethylene naphthalate (PEN) spacers during assembly. For the materials tested in this study, nominal compression was set to 80% of the uncompressed thickness. During assembly, a thin silicone gasket was used to prevent the injected phosphoric acid from circumnavigating the GDL during testing.

A syringe pump (Harvard Apparatus, 11 Plus) was used to control the flow rate of the phosphoric acid into the base of the injection device during breakthrough experiments. An injection flow rate of 5 $\mu l\,h^{-1}$ was applied to minimize the velocity of the phosphoric acid during injection and discourage viscous effects during breakthrough. Phosphoric acid of 85% concentration was used in each case and experiments were performed at room temperature. During the injection process, phosphoric acid pressure was monitored by a pressure transducer (OMEGA PX 309-005A5V0) located upstream of the injection device. Real-time monitoring of the detected pressure was used to identify a flow of phosphoric acid through the auxiliary tubing and injection device. The volume of the sample holder and the tubing system was used to calculate the theoretical instant at which the injected acid reached the sample. Subsequently, μCT snapshots were performed to verify successful penetration of phosphoric acid from the injection point, through the GDL, and into to the channel region of the injection device. Following breakthrough, the inlet of the injection device was sealed.

The injection experiments were conducted at room temperature, and it was assumed that an elevated temperature would have a negligible impact on the intrusion behavior. Evaporation effects are not pronounced at 160 °C, as the vapor phase above hot phosphoric acid contains almost exclusively water [53]. Furthermore, the changes in viscosity of phosphoric acid at high temperature [54] still result in small capillary numbers ($Ca << 1$), which is a precondition to the comparison of the experimental and the simulated invasion pattern, as described later.

2.2. X-ray Micro-Computed Tomography

X-ray μCT scans were used to visualize the phosphoric acid invasion patterns established at breakthrough for each of the GDL materials tested in this study using a desktop μCT machine (Bruker Skyscan 1172). The μCT scans were performed using an X-ray source voltage and current of 36 kV and 222 μA, respectively. Image acquisition settings included a pixel resolution of 2.1 μm per voxel, frame averaging of 4 acquisitions, and a rotational step of 0.28 degrees. Radiographs were collected over 180 degrees of rotation, resulting in the acquisition of 640 individual projections per scan. After collection of these individual projections, the images were reconstructed to recreate the 3D geometry of the GDLs using the NRecon software package. The reconstructed grayscale images were presented in terms of optical density, whereby heavier (more attenuating) materials produce a brighter appearance.

In order to visualize phosphoric acid in the GDLs using μCT, it was first necessary to obtain a "dry" reference state. This reference state was obtained by performing a μCT scan of the assembled injection device prior to performing the phosphoric acid injection experiment. Following completion of this initial scan, the injection procedure defined above was employed to achieve phosphoric acid breakthrough in the GDL. Once breakthrough was established, a final scan was performed in the presence of phosphoric acid to define the "wet" state. Three-dimensional phosphoric acid invasion patterns were then obtained by subtracting the reconstructed geometry defined in the "dry" state from that defined by the "wet" state. Image processing, including manual image registration, subtraction, and the application of a 3D median filter

to remove small, non-physical features in the subtracted image, was performed using Fiji®.

2.3. Pore Network Extraction

The pore network modeling approach used in this study is reliant on first defining the 3D structure of the GDL materials. Using the reconstructed μCT images of the compressed GDL materials that were obtained to establish the "dry" reference state defined above, it was possible to differentiate void, carbon fiber, and MPL voxels. This is achieved through an image processing step called segmentation, in which each voxel in the reconstructed image is assigned to either void, carbon fiber, or MPL. Due to variation in the properties of each phase, different grayscale values were characteristic of each of these phases [55]. The segmentation algorithm employed in this study additionally accounts for the expected volume of each phase based on the manufacturer specified areal densities. Further details concerning the segmentation are detailed in a recent study by Banerjee et al. [56].

Following segmentation, the phase (MPL, carbon fiber, void) differentiated reconstructions of the compressed GDLs were processed to characterize the connected pore network defined by the void voxels. This process is referred to as pore network extraction and has been detailed in a number of studies [21,57]. The extracted 3D pore network characterizes the structural information of the GDL, including pore geometry and interconnectivity. In this 3D network, which is ideally identical to the sample measured in the experiment, the pores are connected by throats to resemble the interconnectivity of the system. The actual pore size and geometry are retained for the simulation, and each pore is assigned a diameter based on the segmented image of the sample, thus resembling the size of the constriction in between two pores of the experimental sample. For the GDL, in which liquid transport is commonly considered to be characteristic of a capillary dominated flow regime [21], the extracted pore network is representative of the GDL. This pore network will further be referred to as an equivalent pore network. The equivalent pore networks were also used to characterize pore size distributions in the tested GDL materials at the tested compression.

2.4. Pore Network Modeling

A pore network modeling approach was employed to simulate the ex situ phosphoric acid breakthrough experiments performed in this study. All simulations were performed using the open-source modeling package, OpenPNM [52]. Specifically, invasion percolation experiments were employed to determine the validity of the assumptions inherent to this modeling approach. The precondition of low capillary numbers ($Ca << 1$) entailed in the simulation of invasion percolation was verified using the following equations:

$$Ca = \frac{U \cdot \eta}{\gamma} \tag{1}$$

$$U = 4 \cdot \frac{\dot{Q}_c}{\pi \cdot d_t^2} \tag{2}$$

where U is the velocity of phosphoric acid in the pores of the sample, η is the viscosity, and γ is the surface tension of phosphoric acid. In Eq. (2), $\dot{Q}_c$ is the applied flow rate of the invasion experiment and d_t is the average throat diameter of the GDL. The values of the phosphoric acid parameters are displayed in Table 2 and were taken from Chevalier et al. [21] and flow rates were reported by Eberhardt et al. [15] Properties of phosphoric acid with a concentration of 90% resulted in capillary numbers in the order of magnitude of 10^{-5} (for both room temperature and elevated temperatures).

To initialize the invasion percolation simulation, an inlet condition was established on the surface of the MPL, or the GDL if, no MPL was present. In our case, the inlet condition entailed the saturation of all pores labeled as 'bottom' (MPL/injection device interface) from which the algorithm started the invasion of pores. In a capillary dominated flow regime and a network consisting of pores connected via throats, the invasion percolation algorithm proceeds with pore filling by comparing the throat diameters for each throat connected to a saturated pore. The throat identified with the lowest entry pressure, corresponding to the largest diameter, will be filled at each step. This procedure is performed iteratively until a predefined end point is reached. In our case this end point is defined as the initial breakthrough event. In the 3D invasion simulation, the first instance at which a pore labeled as 'top' is invaded is identified as the moment of breakthrough. The 'top' boundary is defined at the interface of the GDL and the channel side of the compression device. Once breakthrough is reached, the pathway established by the invasion percolation simulation is assumed to be stable for all operating conditions, as the liquid will further propagate through the path of least resistance in this capillary force dominated regime. The saturation of the bottom layer, corresponding to the initial condition of each simulation, is not shown in the 3D visualizations of the invasion pattern (Fig. 6). However, invaded bottom layer pores are included in the calculation of saturation at breakthrough (Table 3 and Fig. 7). The consideration of a flooded inlet simulates the contact of the GDL with a catalyst layer and is necessary to understand the full impact of an MPL.

The pore network model simulated the MPL as a solid material phase, through which phosphoric acid transport was restricted to macroscopic cracks and holes; consistent with experimental results by Gostick et al. [28], Markötter et al. [31], and Sasabe et al. [32]. Evaporation losses are not considered in the model, as they are believed to be negligibly small with respect to liquid transport in the presence of cracks.

Each crack in the MPL was simulated as a range of connected pores with a diameter equivalent to the width of the crack. These pores were connected by throats with a similar diameter as the pores themselves. This approach entails the proper flow characteristics and ensures proper incorporation of liquid transport through the cracks. The MPL pores, at the interface with the compression device, were labeled as bottom pores and were thus the only entry point for liquids in the simulation.

From the simulation, a detailed quantitative study of network parameters was possible. The pore size distribution inside the porous material, saturation profiles, and capillary pressures were computed based on the invasion simulations. These quantitative numerical results concur the qualitative results from the experimental acid invasion experiment and help to elicit the parameter behind each observed phenomenon. The numerical results serve to explain the occurrence of capillary fingering, bottom-layer invasion (phosphoric acid travels from the acid reservoir and invades the bottom-most pores without protruding further into the sample), and influence of large pores on the invasion pattern. Further, the simulations are applied to investigate the saturation behavior of a GDL in contact with a homogeneously flooded CL. Thus, the impact of the pore size distribution and the MPL on the leaching of acid through the GDL can be explained.

3. Results and Discussion

3.1. Characterization of samples

The manufacturer specifications for the properties of the investigated GDL materials are shown in Table 1. The experimental

Table 1
Manufacturer's data sheet for the investigated materials [60,61]. The substrate porosity reported by the manufacturer is compared with the porosity experimentally determined by analysis of the extracted pore networks of compressed GDL substrates.

Property	SGL 25 BA	SGL 25 BC	Freudenberg H2315	Freudenberg H2315-C2
Thickness [μm]	190	235	210	255
MPL.		☑		☑
MPL thickness [μm]		45		45
Areal weight [g m^{-2}]	40	86	95	135
Manufacturer reported substrate porosity []	0.88		not reported	
Experimentally measured substrate porosity []	0.85		0.66	

Table 2
Parameters of phosphoric acid for calculating the capillary number, adopted from Chevalier et al. [21].

Property	Value
Viscosity, η, [Pa s]	1500
Surface tension, γ, [N m^{-1}]	0.070
Flow rate, $\dot{Q}_c$, [mm^3 s^{-1}]	1.9e-7
Throat diameter, d_t, [μm]	20

average substrate porosity was determined by considering the ratio of solid voxels to void voxels identified by the μCT scans, resulting in particularly strong agreement with the manufacturers specification for SGL 25 BA (+3%). In case of the Freudenberg materials, no porosity value was reported by the manufacturer.

Fig. 2 presents reconstructed images and characteristic physical properties of each GDL to highlight structural differences between them. SGL 25 BA carbon paper is shown to consist of long, straight fibers (Fig. 2a), whereas Freudenberg H2315 exhibits a nonwoven, dense, and tortuous carbon fiber structure, resulting in a higher frequency of small pores (Fig. 2b). These figures also present in-plane slices of the MPL surface for SGL 25 BC and Freudenberg H2315-C2, respectively. The MPL of SGL 25 BC is highly cracked, whereas the MPL of Freudenberg H2315-C2 exhibits minimal irregularities, which rarely penetrate deeply into the MPL when they do exist (confirmed by analysis of reconstructed μCT scans). The presence of cracks in the MPL is suspected to be of significant relevance for fluid transport through the GDL [28,58]. The unique physical properties of these materials lead to distinct variations in pore size distributions (Figs. 2c) and d)). In Fig. 2c), the through plane porosity profile is displayed with the horizontal axis normalized relative to the total thickness of each sample. The experimental average porosity of SGL 25 BA is significantly higher (85%) than that of Freudenberg H2315 (66%). Fig. 2d) quantifies the pore size distributions for each substrate based on analysis of the extracted equivalent pore networks. Freudenberg H2315 exhibits a narrower distribution of smaller pores (mean diameter = 18 μm), whereas SGL 25 BA shows a broad distribution. The mean pore size for SGL 25 BA was 26 μm, with diameters of up to 120 μm detected (Table 3). The largest pores are expected to play a significant role in the distribution of the phosphoric acid, as these pores dominate the flow behavior with their low entry pressures for the injected acid [59]. These materials allow a parametric approach to the investigation of the influence of fiber properties and cracks in the MPL on the distribution and transport of liquid through the GDL.

3.2. Phosphoric acid invasion pattern

The image shown in Fig. 3a) is the result of phosphoric acid injection into SGL 25 BA as detected in the reconstructed grayscale

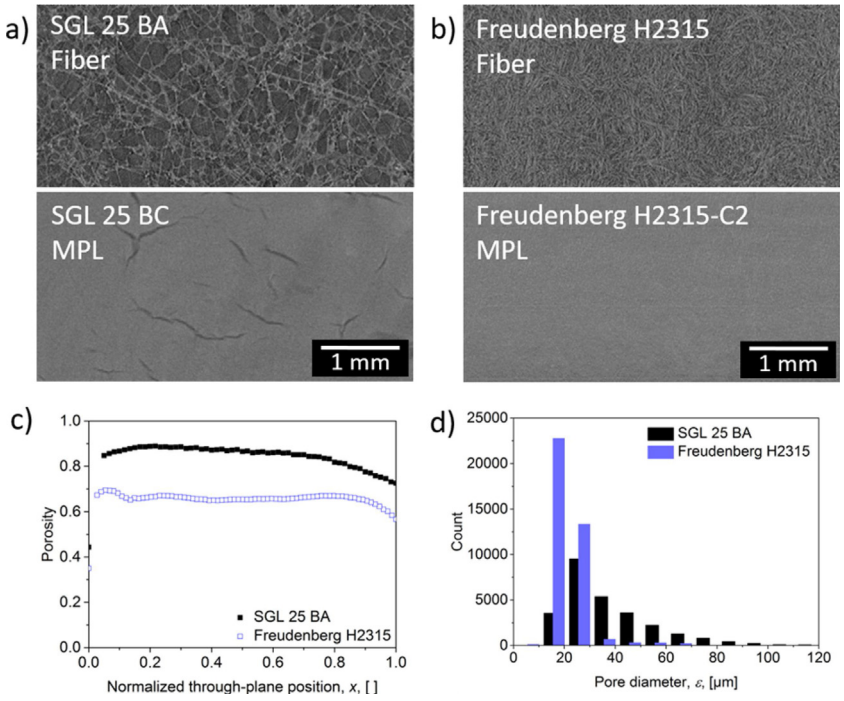

Fig. 2. a) In-plane slice of tomogram for carbon fiber substrate for a) SGL 25 BA and b) Freudenberg H2315. The MPL surface of the respective coated material is shown in the bottom half. c) Through plane porosity profile normalized for the sample thickness obtained by pore network extraction. d) Pore size distribution of SGL 25 BA (black) and Freudenberg H2315 (blue).

Table 3
Properties of the invasion percolation simulations of all investigated materials. The asterisk denotes properties describing only the connected invasion pattern. The saturation at breakthrough considers the flooded inlet condition, simulating contact with the catalyst layer.

	SGL 25 BA	SGL 25 BC (Fiber)	SGL 25 BC (MPL)	Freudenberg H2315
Average pore diameter (all pores) [μm]	26	26	23	18
Average invaded pore diameter [μm]*.	90	65	23	21
Limiting throat diameter [μm]	61	70	57	19
Max. capillary pressure [Pa]	1064	922	1132	3416
Saturation at breakthrough [%]	51.8	4.3		20.8

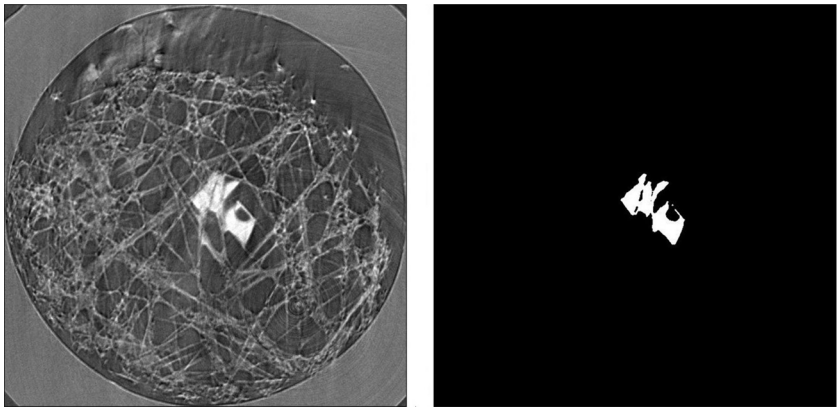

Fig. 3. a) Top view of the 3D μ-CT scan of SGL 25 BA with injected phosphoric acid (circled in red). b) Resulting location and shape of phosphoric acid after image processing.

image and presented in terms of optical density. The bright, white spot in the center (circled in red) is the phosphoric acid flowing through the carbon fiber substrate. After processing the image and extracting the 3D invasion pattern, Fig. 3b) was obtained, showing an in-plane slice of the isolated phosphoric acid. This process was repeated for each sample, except for Freudenberg H2315-C2, for which a successful GDL breakthrough was not obtained. As shown previously in Fig. 2, the MPL of Freudenberg H2315-C2 did not contain cracks, which limited the possibility of acid intrusion into the carbon fiber substrate. Thus, the major phosphoric acid loss mechanism in GDEs containing an ideal crack-free MPL is expected to be the evaporation loss. Especially at high humidification rates, many start- stop cycles, and high current densities, gaseous phosphoric acid transport rates will be increased and in long-term operation, the gas transport through the nano pores will contribute to the degradation.

Fig. 4 provides visualizations of the invasion patterns for three successful breakthrough experiments performed with SGL 25 BA, SGL 25 BC, and Freudenberg H2315. Several properties of the phosphoric acid breakthrough pattern can be investigated via the 3D visualizations. The invasion pattern illustrates how the acid progressed through the material and properties like capillary fingering or bottom-layer invasion can be visualized.

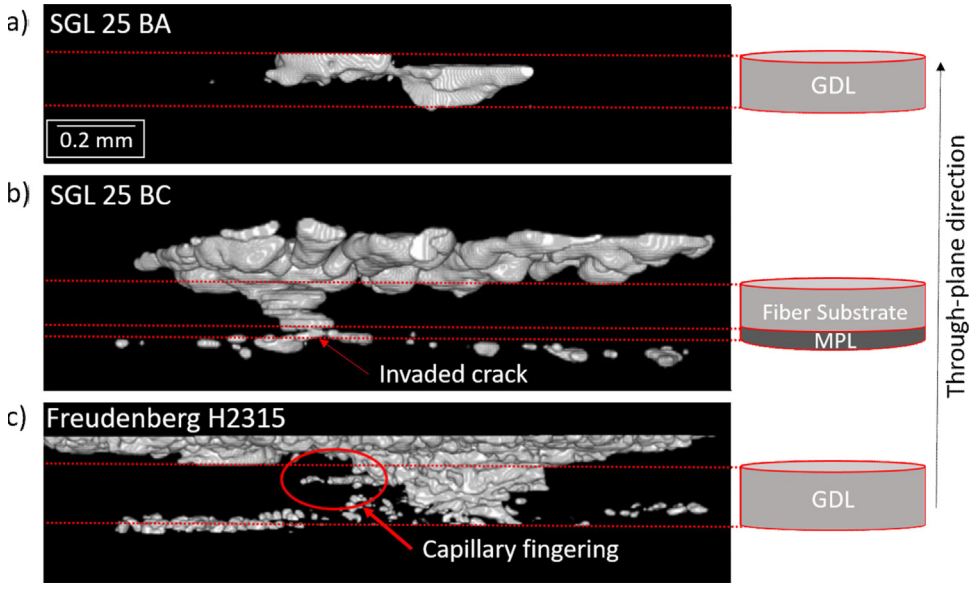

Fig. 4. Experimental phosphoric acid invasion patterns obtained from 3D μCT scans performed during injection experiments for a) SGL 25 BA, b) SGL 25 BC, and c) Freudenberg H2315. The scheme of the samples on the right is to scale only in through plane direction.

The invasion pattern through SGL 25 BA consisted of two invaded pore spaces which were connected via one constriction (throat). The sizes of the pores were large compared to the total thickness of the compressed sample (117.3 μm pore diameter vs. 152 μm sample thickness, determined by pore network modeling), as seen in Fig. 4a). A straight, non-divergent pathway is to be expected in a carbon fiber material like SGL 25 BA due to the presence of large pores, consequently capillary fingering is unlikely. Fig. 4b) shows the phosphoric acid invasion pattern in SGL 25 BC. With the introduction of an MPL, the resistance to the invasion of phosphoric acid increases as the sample is unlikely to have a large inlet pore directly above the injection point. Thus, acid is forced to migrate along the MPL interface of the sample until it reaches a crack, which constitutes a potential inlet into the sample. Once a crack is invaded, the acid again penetrates the substrate in a non-divergent way. The injection experiment for SGL 25 BC was not stopped at the exact moment of breakthrough causing acid to flood the channel region above the top of the sample, as seen in Fig. 4b). This observation further validates the assumption that a stable pathway through the sample is reached after breakthrough.

In Fig. 4c) the breakthrough pattern for Freudenberg H2315 is shown. The maximum capillary pressure reached in this test (3416 Pa) was high enough to cause capillary fingering. Further, the absence of an MPL allows several pores on the bottom side of the sample to be invaded before a stable breakthrough pattern is formed. The capillary pressures associated with the relatively small pore and throat sizes (Table 3) in Freudenberg H2315 caused acid migration beneath the sample before the event of breakthrough.

3.3. Liquid flow through cracks in the MPL

Fig. 5 presents in-plane views of the MPL interface for SGL 25 BC to highlight the similarity between the grayscale image obtained form μCT measurements (Fig. 5a) and c)) our extracted pore network (Fig. 5b) and d)). Fig. 5c) highlights phosphoric acid invading a crack in the MPL of SGL 25 BC. From this crack, phosphoric acid invaded further into the carbon fiber substrate, eventually reaching breakthrough. In the model, the largest pores located in the MPL cracks were up to 60 μm in diameter and played a significant role in the overall invasion characteristics of the material. The majority of pores identified in the cracks of the MPL were between 20 and 30 μm in diameter.

3.4. Simulation of phosphoric acid intrusion

The simulation of acid invasion into the experimental samples demonstrates qualitative agreement with the experimental results and identifies the ability of the model to predict pathway characteristics. Fig. 6 shows the invasion patterns resulting from invasion percolation simulations of phosphoric acid injection into the three GDL samples. On the right side of Fig. 6, a magnified representation of the pores within the carbon fiber substrate leading to breakthrough is shown. The invasion pattern established by phosphoric acid in SGL 25 BA consists of identical pores as were invaded in the injection experiment. This was determined by comparing the coordinates of the invasion in both the experiment and the simulation. In each case, the breakthrough pattern consists of only two large pores connected by one throat.

In case of SGL 25 BC, few cracks in the MPL were invaded before the acid penetrated the carbon fiber substrate. The discrete nature of MPL cracks and reduced pore size in the MPL limit potential intrusions of phosphoric acid into the carbon fiber substrate. The pore coordinates of the simulation and the experiment in SGL 25 BC did not match, as they did in case of SGL 25 BA. This discrepancy is caused by the inlet condition of the algorithm, which saturated all the cracks simultaneously, from where the invasion of phosphoric acid into the carbon fiber substrate was initiated. However, this is not the case in the experiment, where the intrusion of phosphoric acid is limited to the invasion of a crack during the acid migration beneath the sample. Thus, the invasion did not start from the largest crack, as it did in the simulation.

The invasion pattern obtained for Freudenberg H2315 exhibits strong qualitative correlations to the experimental results. In both the experimentally and numerically obtained breakthrough patterns for Freudenberg H2315, capillary fingering was observed. A second concurrent phenomenon is the bottom-layer invasion in the sample. This is more pronounced in the simulation, which can be attributed to minor differences in the boundary condition which occurs at the MPL interface.

The results presented in Table 3 and Fig. 7 are computed within OpenPNM and help to understand the parameters behind the occurrence of the observed characteristics in the invasion patterns. Average pore diameters, capillary pressures, and saturation values are listed in Table 3. The mean pore diameter of the MPL of SGL 25 BC is in the same order of magnitude (difference of 13%) as the

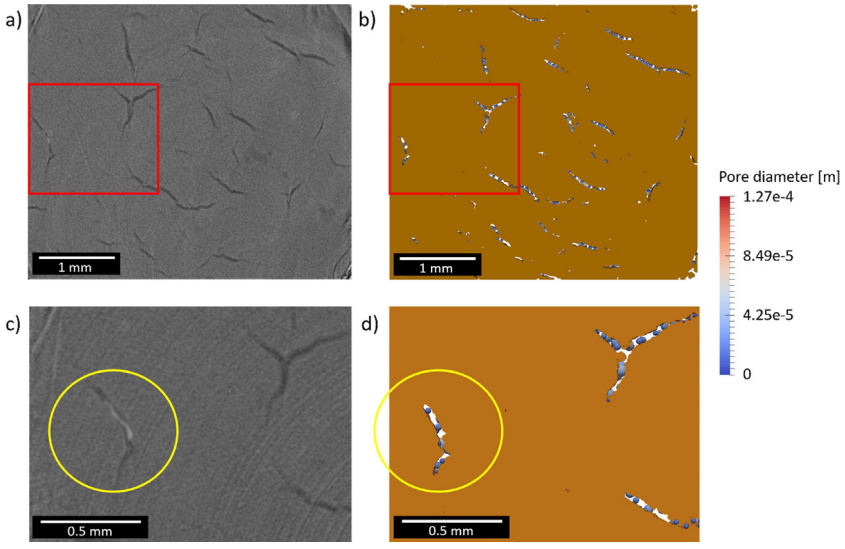

Fig. 5. a) and c) show μCT images of the MPL of SGL 25 BC, b) and d) show the equivalent pore network of the same regions. Figure c) also emphasizes the flow of phosphoric acid through a crack in the MPL during injection experiments.

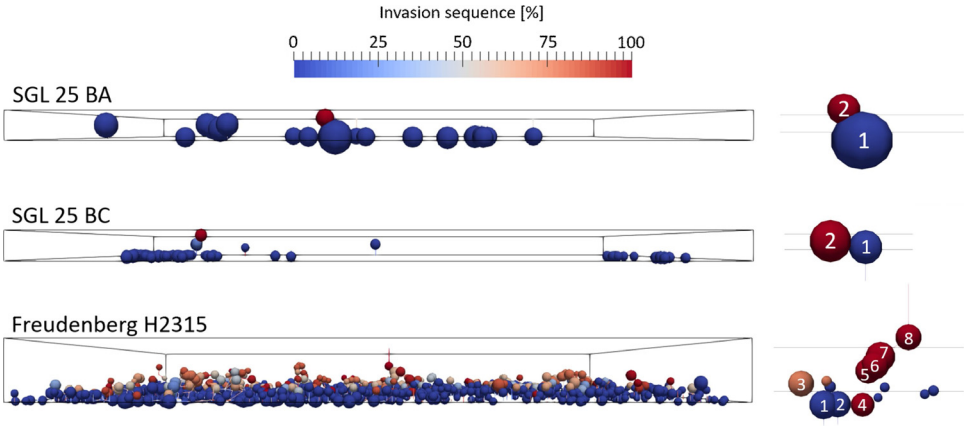

Fig. 6. Side view of the phosphoric acid distribution in the investigated materials obtained by pore network modeling. A magnification of the breakthrough pattern is reported on the right side of each figure. Each pore which is part of the invasion pattern leading to breakthrough was labelled chronologically by their number in the invasion sequence. Each sample has an edge length of 2.1 mm. The size of the pores is corresponding to their pore diameter; the color denotes the invasion sequence.

mean pore diameter of the substrate, indicating that the width of the cracks is similar to the pore diameters in the substrate. Freudenberg H2315 exhibits smaller pores, resulting in a size difference of 44% compared to the SGL carbon substrate.

The effect of the breadth of the pore size distribution is highlighted in the average invaded pore diameter. Herein, the impact of the largest pores (>70 μm) on the invasion pattern becomes visible, as they dominate the flow behavior by establishing stable breakthrough patterns quickly. A narrower pore size distribution, as exhibited by Freudenberg H2315, forces phosphoric acid to invade narrower pores and throats, thus increasing the capillary pressure significantly. The capillary pressure of the Freudenberg material is larger by a factor of three when compared to both SGL materials, causing capillary fingering and bottom-layer invasion.

Lastly, the saturation at breakthrough was calculated by simulating contact with a flooded catalyst layer. The smaller average pore diameter and the narrow pore size distribution of Freudenberg H2315 results in a significantly decreased saturation at breakthrough compared to SGL 25 BA (20.8% vs. 51.8%). This effect was dominated by the presence of an MPL in SGL 25 BC. By physically blocking the invasion of large bottom pores in the carbon fiber substrate, the MPL decreased the saturation to 4.3%, largely impacting the flow behavior in the material.

Fig. 7 quantitatively displays the effect of the MPL on the saturation of pores in the materials, simulating contact with a flooded CL in contrast to the experimental point injection. This is the reason why the modeled saturation profiles exhibit high saturation values at low through-plane positions. a) and b) show the fraction of invaded pores with respect to the total number of pores. 35% of pores in SGL 25 BA were invaded, compared to only 5% in SGL 25 BC. Fig. 7c) highlights the difference between the invaded pores in both materials, showing that the MPL most strongly affects the invasion of large pores (>50 μm). This plays a role in Fig. 7d), where the saturation of both materials is shown. The saturation of SGL 25 BC is universally lower than that of SGL 25

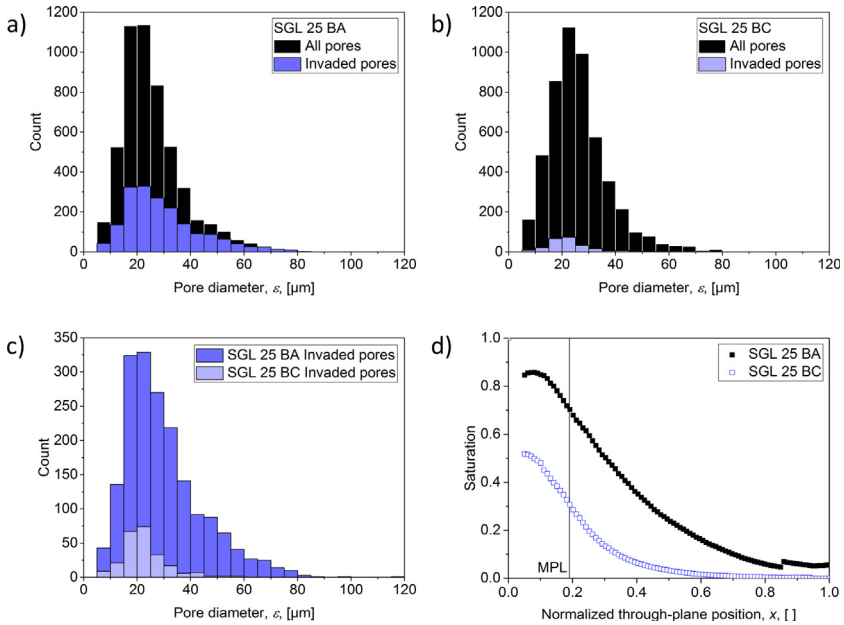

Fig. 7. Pore size distributions of SGL 25 BA (a) and SGL 25 BC (b) obtained from OpenPNM. The pores invaded at breakthrough are highlighted in light blue, the entirety of pores is shown in black. c) A comparison of the number of invaded pores at the moment of breakthrough. d) The influence of an MPL on the saturation profile.

BA, suggesting that the MPL is vital to limit mass transport losses due to gas diffusion layer flooding in contact with a flooded catalyst layer.

4. Concluding remarks

In this work, phosphoric acid was injected into several GDL samples in order to visualize the 3D invasion pathways and identify the effect of the GDL structure on the shape of the pathway. Further, pore network modeling was applied to investigate qualitative information from the phosphoric acid invasion pattern into GDLs and to quantify properties of phosphoric acid transport through a porous carbon fiber substrate, such as limiting throat diameters and maximum capillary pressures. Particular effort was made to identify the effect of the GDL structure on the shape of the invasion pattern in order to augment the understanding of phosphoric acid transport through porous material.

Experimental injection of phosphoric acid into a GDL containing an MPL gave strong evidence of liquid transport through the cracks of an MPL. An MPL also dictates the intrusion points of phosphoric acid into the underlying carbon fiber by physically blocking intrusion. The experimental injection of phosphoric acid into a crack-free MPL did not result in a breakthrough pattern, this further suggests that MPL cracks provide preferential pathways for phosphoric acid.

Further, we found that denser carbon fiber structures facilitate a divergent invasion pattern and that smaller pore sizes increase the capillary pressure, which results in bottom layer invasion and branching of the invasion pattern. The saturation of carbon fibers with a smaller pore size and a narrower pore diameter distribution (20.8%) is significantly lower than the saturation of a material consisting of larger pores (51.8%). However, the pore size effect on the saturation was less pronounced than the effect of the MPL, which decreased the saturation to 4.3%.

Large cracks and high substrate porosity, resulting in larger pores, are beneficial to maintain low capillary pressures and establishing a locally confined pathway through the GDE. In HT-PEMFCs, the MPL is required to inhibit the liquid transport of phosphoric acid out of the cell, thus a crack-free and thick MPL on a substrate with small pores is beneficial to retaining the acid inside the catalyst layer during operation. The dominating acid loss mechanism in such an MPL is evaporation, especially at irregular operating conditions and high current densities.

This work presents the validation of pore network modeling to simulate the flow of phosphoric acid through GDLs. Within the conditions of the custom-built injection device, the location and the breakthrough pattern of phosphoric acid was reconstructed, and the main characteristics of flow patterns could be qualitatively determined.

Acknowledgements

Financial support from the Natural Sciences and Engineering Research Council of Canada (NSERC), the NSERC Discovery Accelerator Program, the NSERC Canada Research Chairs Program, the Ontario Ministry of Research and Innovation Early Researcher Award, and the Canada Foundation for Innovation are gratefully acknowledged. Graduate scholarships received by M. G. George from the NSERC Canada Graduate Scholarship (CGS) and the Ontario Graduate Scholarship (OGS) are also gratefully acknowledged. Further, we greatly acknowledge the “Impuls- und Vernetzungsfonds der Helmholtz Gesellschaft” for the financial support (Young Investigator Group project VH-NG-616) and the PROMOS – “Programm zu Steigerung der Mobilität von Studierenden deutscher Hochschulen” funding program granted by the DAAD for financial support. The authors would like to thank Prof. M. T, Kortschot and Shiang Law in the Department of Chemical Engineering & Applied Chemistry and Prof. Mohini M. Sain in the Faculty of Forestry at the University of Toronto for the use of the microcomputed tomography facilities.

References

[1] H. Li, Y. Tang, Z. Wang, Z. Shi, S. Wu, D. Song, J. Zhang, K. Fatih, J. Zhang, H. Wang, Z.-S. Liu, R. Abouatallah, A. Mazza, A review of water flooding issues in the proton exchange membrane fuel cell, J. Power Sources 178 (2008) 103–117.
[2] Y. Wang, K.S. Chen, J. Mishler, S.C. Cho, X. Cordobes Adroher, A review of polymer electrolyte membrane fuel cells: Technology, applications, and needs on fundamental research, Applied Energy 88 (2011) 981–1007.
[3] F. Bresciani, A. Casalegno, G. Varisco, R. Marchesi, Water transport into PEFC gas diffusion layer: experimental characterization of diffusion and permeation, Int. J. Energy Res. 38 (2014) 602–613.
[4] J. Mengbo, Z. Wei, A Review of Water Management in Polymer Electrolyte Membrane Fuel Cells, Energies 2 (2009) 1057–1106.
[5] Z. Qi, C. He, A. Kaufman, Effect of CO in the anode fuel on the performance of PEM fuel cell cathode, J. Power Sources 111 (2002) 239–247.
[6] M. Boaventura, I. Alves, P. Ribeirinha, A. Mendes, The influence of impurities in high temperature polymer electrolyte membrane fuel cells performance, Int. J. Hydrogen Energy (2016) 10.
[7] T.J. Schmidt, J. Baurmeister, Durability and reliability in high-temperature reformed hydrogen PEFCs, ECS Transactions 3 (2006) 861–869.
[8] R. Zeis, Materials and characterization techniques for high-temperature polymer electrolyte membrane fuel cells, Beilstein Journal of Nanotechnology 6 (2015) 68–83.
[9] J. Zhang, Z. Xie, J. Zhang, Y. Tang, C. Song, T. Navessin, Z. Shi, D. Song, H. Wang, D. P. Wilkinson, Z.-S. Liu, S. Holdcroct, High temperature PEM fuel cells, J. Power Sources 160 (2006) 872–891.
[10] S. Malhotra, R. Datta, Membrane-Supported Nonvolatile Acidic Electrolytes Allow Higher Temperature Operation of Proton-Exchange Membrane Fuel Cells, J. Electrochem. Soc. 144 (1997) L23–L26.
[11] Q. Li, R. He, J.O. Jensen, N.J. Bjerrum, PBI-Based Polymer Membranes for High Temperature Fuel Cells – Preparation, Characterization and Fuel Cell Demonstration, Fuel Cells 3 (2004) 147–159.
[12] J. Zhang, Y. Tang, C. Song, J. Zhang, Polybenzimidazole-membrane-based PEM fuel cell in the temperature range of 120–200 °C, J. Power Sources 172 (2007) 163–171.
[13] F. Mack, S. Heissler, R. Laukenmann, R. Zeis, Phosphoric acid distribution and its impact on the performance of polybenzimidazole membranes, J. Power Sources 270 (2014) 627–633.
[14] J.S. Wainright, J.-T. Wang, D. Weng, R.F. Savinell, M. Litt, Acid-Doped Polybenzimidazoles: A New Polymer Electrolyte, J. Electrochem. Soc. 142 (1995) L121–L123.
[15] S.H. Eberhardt, F. Marone, M. Stampanoni, F.N. Büchi, T.J. Schmidt, Operando X-ray Tomographic Microscopy Imaging of HT-PEFC: A Comparative Study of Phosphoric Acid Electrolyte Migration, J. Electrochem. Soc. 163 (2016) F842–F847.
[16] Y. Oono, A. Sounai, M. Hori, Influence of the phosphoric acid-doping level in a polybenzimidazole membrane on the cell performance of high-temperature proton exchange membrane fuel cells, J. Power Sources 189 (2009) 943–949.
[17] F. Mack, T. Morawietz, R. Hiesgen, D. Kramer, V. Gogel, R. Zeis, Influence of the polytetrafluoroethylene content on the performance of high-temperature polymer electrolyte membrane fuel cell electrodes, Int. J. Hydrogen Energy 41 (2016) 7475–7483.
[18] K. Kwon, T.Y. Kim, D.Y. Yoo, S.-G. Hong, J.O. Park, Maximization of high-temperature proton exchange membrane fuel cell performance with the optimum distribution of phosphoric acid, J. Power Sources 188 (2009) 463–467.
[19] K. Kwon, J.O. Park, D.Y. Yoo, J.S. Yi, Phosphoric acid distribution in the membrane electrode assembly of high temperature proton exchange membrane fuel cells, Electrochim. Acta 54 (2009) 6570–6575.
[20] M. Boaventura, A. Mendes, Activation procedures characterization of MEA based on phosphoric acid doped PBI membranes, Int. J. Hydrogen Energy 35 (2010) 11649–11660.
[21] S. Chevalier, M. Fazeli, F. Mack, S. Galbiati, I. Manke, A. Bazylak, R. Zeis, Role of the microporous layer in the redistribution of phosphoric acid in high temperature PEM fuel cell gas diffusion electrodes, Electrochim. Acta 212 (2016) 187–194.
[22] S.H. Eberhardt, M. Toulec, F. Marone, M. Stampanoni, F.N. Büchi, T.J. Schmidt, Dynamic Operation of HT-PEFC: In-Operando Imaging of Phosphoric Acid Profiles and (Re)distribution, J. Electrochem. Soc. 162 (2015) F310–F316.
[23] C. Wannek, I. Konradi, J. Mergel, W. Lehnert, Redistribution of phosphoric acid in membrane electrode assemblies for high-temperature polymer electrolyte fuel cells, Int. J. Hydrogen Energy 34 (2009) 9479–9485.
[24] P. Alnegren, J.G. Grolig, J. Ekberg, G. Göransson, J.-E. Svensson, Metallic Bipolar Plates for High Temperature Polymer Electrolyte Membrane Fuel Cells, Fuel Cells 16 (2015) 39–45.
[25] C. Hartnig, T.J. Schmidt, On a new degradation mode for high-temperature polymer electrolyte fuel cells: How bipolar plate degradation affects cell performance, Electrochim. Acta 56 (2011) 4237–4242.

[26] S. Yu, L. Xiao, B.C. Benicewicz, Durability Studies of PBI-based High Temperature PEMFCs, Fuel Cells 3–4 (2008) 165–174.
[27] J. Lee, J. Hinebaugh, A. Bazylak, Synchrotron X-ray radiographic investigations of liquid water transport behavior in a PEMFC with MPL-coated GDLs, J. Power Sources 227 (2013) 123–130.
[28] J.T. Gostick, M.A. Ioannidis, M.A. Fowler, M.D. Pritzker, On the role of the mocroporous layer in PEMFC operation, Electrochem. Commun. 11 (2009) 576–579.
[29] P. Deevanhxay, T. Sasabe, S. Tsushima, S. Hirai, Observation of dynamic liquid water transport in the microporous layer and gas diffusion layer of an operating PEM fuel cell by high-resolution soft X-ray radiography, J. Power Sources 230 (2013) 38–43.
[30] Z. Lu, M.M. Daino, C. Rath, S.G. Kandlikar, Water management studies in PEM fuel cells, part III: Dynamic breakthrough and intermittent drainiage characteristics from GDLs with and without MPLs, Int. J. Hydrogen Energy 35 (2010) 4222–4233.
[31] H. Markötter, I. Manke, P. Krüger, T. Arlt, J. Haussmann, M. Klages, H. Riesemeier, C. Hartnig, J. Scholta, J. Banhart, Investigation of 3D water transport paths in gas diffusion layers by combined in-situ synchrotron X-ray radiography and tomography, Electrochem. Commun. 13 (2011) 1001–1004.
[32] T. Sasabe, P. Deevanhxay, S. Tsushima, S. Hirai, Soft X-ray visualization of the liquid water transport within the cracks of micro porous layer in PEMFC, Electrochem. Commun. 13 (2011) 638–641.
[33] M. Mortazavi, K. Tajiri, Liquid water breakthrough pressure thorugh gas diffusion layer of proton exchange membrane fuel cell, Int. J. Hydrogen Energy 39 (2014) 9409–9419.
[34] J. Lobato, P. Cañizares, M.A. Rodrigo, D. Úbeda, F.J. Pinar, J.J. Linares, Optimisation of the Microporous Layer for a Polybenzimidazole-Based High Temperature PEMFC – Effect of Carbon Content, Fuel Cells 5 (2010) 770–777.
[35] S. Chevalier, N. Ge, M.G. George, J. Lee, R. Banerjee, H. Liu, P. Shrestha, D. Muirhead, J. Hinebaugh, Y. Tabuchi, T. Kotaka, Synchrotron X-ray radiography as a highly precise and accurate method for measuring the spatial distribution of liquid water in operating polymer electrolyte membrane fuel cells, J. Electrochem. Soc. 164 (2) (2017) Jan 1 F107-14.
[36] J. Eller, J. Roth, F. Marone, M. Stampanoni, F.N. Büchi, Operando Properties of Gas Diffusion Layers: Saturation and Liquid Permeability, J. Electrochem. Soc. 164 (2017) F115–F126.
[37] J. Lee, S. Chevalier, R. Banerjee, P. Antonacci, N. Ge, R. Yip, T. Kotaka, Y. Tabuchi, A. Bazylak, Investigating the effects fo gas diffusion layer substrate thickness on polymer electrolyte membrane fule cell performance via synchrotron X-ray radiography, Electrochim. Acta 236 (2017) 161–170.
[38] D.S. Hussey, D.L. Jacobson, M. Arif, J.P. Owejan, J.J. Gagliardo, T.A. Trabold, Neutron images of the through-plane water distribution of an operating PEM fuel cell, J. Power Sources 172 (2007) 225–228.
[39] P. Boillat, J. Biesdorf, P. Oberholzer, A. Kaestner, T.J. Schmidt, Evaluation of Neutron Imaging for Measuring Phosphoric Acid Distribution in High Temperature PEFCs, J. Electrochem. Soc. 161 (2014) F192–F198.
[40] S. Galbiati, A. Baricci, A. Casalegno, R. Marchesi, Sensitivity analysis of a polybenzimidazole-based polymer fuel cell and insight into the effect of humidification, Int. J. Energy Res. 38 (2013) 780–790.
[41] N. Djilali, Computational modelling of polymer electrolyte membrane (PEM) fuel cells: Challenges and opportunities, Energy 32 (2007) 269–280.
[42] S.H. Eberhardt, T. Lochner, F.N. Büchi, T.J. Schmidt, Correlating Electrolyte Inventory and Lifetime of HT-PEFC by Accelerated Stress Testing, J. Electrochem. Soc. 162 (2015) F1367–F1372.
[43] M. Kim, T. Kang, J. Kim, Y.-J. Sohn, One-dimensional modeling and analysis for performance degradation of high temperature proton exchange membrane fuel cell using PA doped PBI membrane, Solid State Ionics 262 (2014) 319–323.
[44] A. Baricci, M. Zago, A. Casalegno, A quasi 2D Model of a High Temperature Polymer Fuel Cell for the Internpretation of Impedance Spectra, Fuel Cells 6 (2014) 926–937.
[45] D.G. Caglayan, B. Sezgin, Y. Devrim, I. Eroglu, Three-dimensional modeling of a high temperature polymer electrolyte membrane fuel cell at different operation temperatures, Int. J. Hydrogen Energy 41 (2016) 10060–10070.
[46] M. Aghighi, M.A. Hoeh, W. Lehnert, M. Geraldine, J. Gostick, Simulation of a Full Fuel Cell Membrane Electrode Assembly Using Pore Network Modeling, J. Electrochem. Soc. 163 (2016) F384–F392.
[47] E.F. Medici, I.V. Zenyuk, D.Y. Parkinson, A.Z. Weber, J.S. Allen, Understanding Water Transport in Polymer Electrolyte Fuel Cell Using Coupled Continuum and Pore-Network Models, Fuel Cells (2016) 9.
[48] M. Fazeli, J. Hinebaugh, A. Bazylak, Investigating Inlet Condition Effects on PEMFC GDL Luquid Water Transport through Pore Network Modeling, J. Electrochem. Soc. 162 (2015) F661–F668.
[49] M. Fazeli, J. Hinebaugh, Z. Fishman, C. Tötzke, W. Lehnert, I. Manke, A. Bazylak, Pore network modeling to explore the effects of compression on multiphase transport in polymer electrolyte membrane fuel cell gas diffusion layers, J. Power Sources 335 (2016) 162–171.
[50] J.T. Gostick, Random Pore Network Modeling of Fibrous PEMFC Gas Diffusion Media Using Voronoi and Delaunay Tessellations, J. Electrochem. Soc. 160 (2013) F731–F743.
[51] J.T. Gostick, M.A. Ioannidis, M.A. Fowler, M.D. Pritzker, Pore network modeling of fibrous gas diffusion layer for polymer electrolyte membrane fuel cells, J. Power Sources 173 (2007) 277–290.
[52] J. Gostick, M. Aghighi, J. Hinebaugh, T. Tranter, M.A. Hoeh, H. Day, B. Spellacy, M.H. Sharqawy, A. Bazylak, A. Burns, W. Lehnert, A. Putz, OpenPNM: A Pore Network Modeling Package, Comput. Sci. Eng. 18 (2016) 60–74.
[53] E.H. Brown, C.D. Whitt, Vapor Pressure of Phosphoric Acids, Ind. Eng. Chem. 44 (1951) 615–618.
[54] PotashCorp, Purified phosphoric acid: Technical information bulletin, (2012) .
[55] N. Otsu, A Threshold Selection Method from Grey-Level Histograms, IEEE Trans. Syst. Man Cyb. SMC-9 (1979) 62–66.
[56] R. Banerjee, J. Hinebaugh, H. Liu, R. Yip, N. Ge, A. Bazylak, Heterogeneous porosity distributions of polymer electrolyte membrane fuel cell gas diffusion layer materials with rib-channel compression, Int. J. Hydrogen Energy 41 (2016) 14885–14896.
[57] M. Fazeli, J. Hinebaugh, A. Bazylak, Incorporating Embedded Microporous Layers into Topologically Equivalent Pore Network Models for Oxygen Diffusivity Calculations in Polymer Electrolyte Membrane Fuel Cell Gas Diffusion Layers, Electrochim. Acta 216 (2016) 364–375.
[58] T. Suzuki, S. Tsushima, S. Hirai, Microscopic Analysis of Interlayer Structure and Oxygen Transport Behaviors in Porous Electrode in PEMFC, ECS Transactions 58 (2013) 489–494.
[59] C.S. Kong, D.-Y. Kim, H.-K. Lee, Y.-G. Shul, T.-H. Lee, Influence of pore-size distribution of diffusion layer on mass-transport problems of proton exchange membrane fuel cells, J. Power Sources 108 (2002) 185–191.
[60] SGL Group, The Carbon Company: Technical data sheet, (2009) .
[61] Freudenberg Company: Technical data sheet, 2014.